

Chimie douce synthesis and thermochemical characterization of mesoporous perovskite-type titanate phases

Laura Bocher, Myriam H. Aguirre, Rosa Robert, Matthias Trottmann, Dmitry Logvinovich, Paul Hug, Anke Weidenkaff*

Empa, Swiss Federal Laboratories for Materials Testing and Research, Solid State Chemistry and Catalysis, Überlandstrasse 129, CH-8600 Dübendorf, Switzerland

Received 21 September 2006; received in revised form 15 February 2007; accepted 19 February 2007
Available online 27 February 2007

Abstract

Various compositions of perovskite-type titanates were synthesised by a *chimie douce* synthesis method with emphasis on low synthesis temperatures. The cations were complexed by citric acid as chelating agent forming a homogeneous organic/inorganic network. The thermal decomposition of this xerogel precursor was investigated by thermogravimetric analysis (TGA). Simultaneous thermal analysis with mass spectrometry (MS) in combination with infrared spectroscopy (IR) allowed studying the precursor decomposition mechanism. The perovskite phase formation was investigated by X-ray diffraction (XRD) and transmission electron microscopy (TEM). The citrate precursor was decomposed by two different preparation methods to evaluate the influence on the morphology and size of perovskite-type particles. The perovskite-type titanates obtained by thermal decomposition of precursors revealed well-defined mesoporous morphology. Ultrafine perovskite-type particles were also synthesized inside micro-droplets in an aerosol process using ultrasonic spray combustion (USC). This alternative preparation enhanced the specific surface area particles by a factor 3 reaching 50–60 m²/g.

© 2007 Elsevier B.V. All rights reserved.

Keywords: Perovskite-type titanate phases; Citrate-complex precursor; Thermal decomposition; Microstructure; Morphology

1. Introduction

Perovskite-type phases are well-known to offer attractive physical and chemical properties [1] such as colossal magnetoresistance (CMR) [2], thermoelectricity [3,4] or catalytic activity [5].

Thermoelectric materials based on the perovskite-type structure reveal an increasing scientific interest in the last years [6]. Perovskite-type materials exhibit attractive thermoelectric properties because of their interesting electronic structure. These oxides are appropriate thermoelectric materials for a large range of temperature due to their chemical and thermal stability. The thermoelectric activity is described by the so-called Figure of Merit, ZT (where $Z = S^2\sigma/\kappa$, S is the Seebeck coefficient, σ and κ are the electrical and thermal conductivities, respectively) [7]. Large Seebeck coefficients and high electrical conductivities are observed for several perovskite-type manganate, titanate or

cobaltate phases [8–10]. A compromise between high power factor ($S^2\sigma$) and low thermal conduction is required to optimise ZT . The thermal transport in a solid is dominated by the motions of electrons and phonons [11]. The total thermal conductivity is defined by the sum of the electronic (κ_e) and the lattice (κ_L) contributions. The electronic contribution is directly related to the electrical conductivity by the Wiedemann–Franz law [12]. The lattice heat conduction can be reduced by phonon scattering by different scattering mechanisms. A challenge is the lowering of the lattice thermal conductivity by reducing the grain size of the particles. Small grain size enhances the phonon scattering due to the grain boundary scattering [11]. Moreover, composition and morphology influence the electronic structure of the perovskite-type phases. The flexible crystallographic structure of the perovskite allows to tune the properties of the material. Suitable cationic substitutions of the same oxide matrix lead to hole- or electron-type doping. Thus, an all oxide thermoelectric generator can be realised combining p- and n-type oxide semiconductors [13].

Transition metal oxides as ABO_3 ($A = \text{Ln, Ca, Sr, Ba}$ and $B = \text{Co, Mn, Ni}$) are also promising materials for catalytic

* Corresponding author. Tel.: +41 44 823 41 31; fax: +41 44 823 40 34.
E-mail address: anke.weidenkaff@empa.ch (A. Weidenkaff).

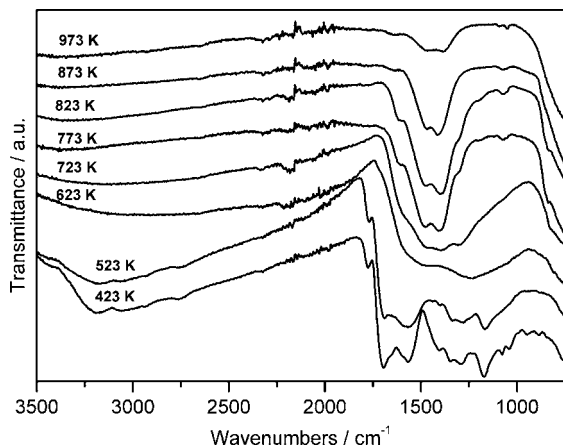


Fig. 1. Infrared spectra of (La,Ca)-Ti citrate precursors heat treated at different temperatures.

processes (e.g. waste gas purification) [14]. The catalytic activity depends on the structure and composition of the selected materials where the valence states and the vacancies are playing an important role. The morphology of the oxide particles influences also the catalytic reactivity which can be enhanced with a larger exposed surface area. Thus, nanosized porous morphologies can be appropriate for catalytic applications [15]. The morphology as well as the particle size can be controlled by the synthesis process leading to the perovskite particles [16,17].

The present work shows the impact of different preparation methods for perovskite-type titanate phases based on the *chimie douce* synthesis route. A molecular network between citric acid as chelating ligand and metals forms the citrate precursor solution [18,19]. A controlled bulk thermal decomposition of the precursor leads to smaller particle size and therefore improved reactivity. Pure perovskite phases with different compositions are achieved at low synthesis temperature. Optimum synthesis conditions have to be defined to obtain phase purity as well as the desired morphology and composition. Systematic investigations on the precursor have been performed to understand the decomposition mechanism and the microstructural properties. Ultrafine perovskite particles were produced as well from citrate-complex

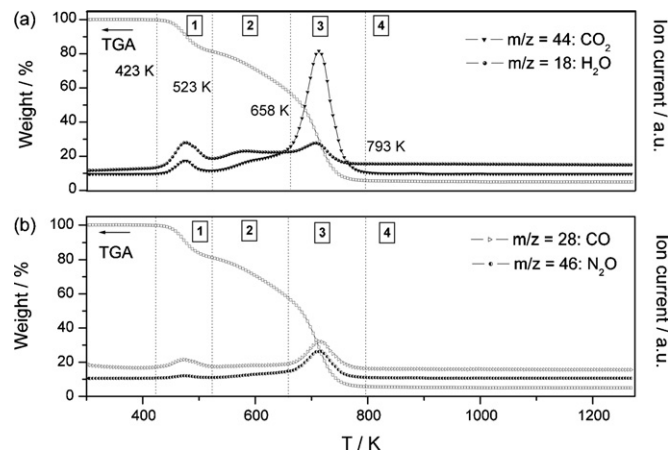


Fig. 3. TGA and MS signals (in synthetic air, 2 K/min) of (La,Ca)-Ti citrate precursor (predried at $T = 423$ K). (a) MS plots— m/z 44: CO_2 and m/z 18: H_2O and (b) MS plots— m/z 28: CO , m/z 46: NO_2 (enlarged).

decomposition using the ultrasonic spray combustion (USC) process.

2. Experimental

The perovskite-type titanate phases $\text{La}_{1-x}\text{Ca}_x\text{TiO}_{3-\delta}$ ($x = 0.3; 0.5; 0.7$) were prepared by solid-state reactions and by *chimie douce* synthesis routes. Either stepwise calcinations (bulk method) or a continuous combustion process (ultrasonic spray combustion) were used to decompose the corresponding citrate precursor prepared by *chimie douce* synthesis route. (All chemicals were purchased from Merck unless otherwise noted.)

With solid-state reaction method, polycrystalline powders were obtained by mixing stoichiometric amounts of La_2O_3 ($\geq 99.99\%$), CaO ($\geq 97\%$) and TiO_2 ($\geq 99.99\%$). The mixture was calcined at 1673 K for 48h including intermediate grindings.

For the *chimie douce* synthesis route, Ti metal powder (Alfa Aesar, $\geq 99.99\%$) was dissolved as described by Camargo et

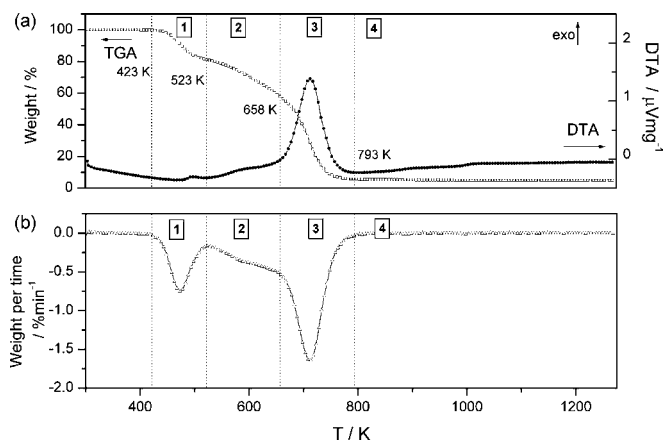


Fig. 2. (a) TGA/DTA curves and (b) DTG curve (in synthetic air, 2 K/min) of (La,Ca)-Ti citrate precursor (predried at $T = 423$ K).

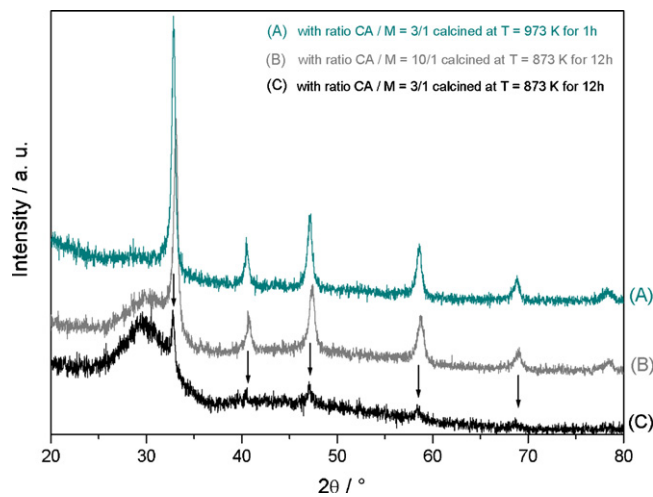


Fig. 4. X-ray diffractograms of $\text{La}_{0.5}\text{Ca}_{0.5}\text{TiO}_{3-\delta}$ prepared with different (CA/M) molar ratio and calcined at different temperatures and times. Reflections are indexed based on orthorhombic structure (space group: $Pnma$).

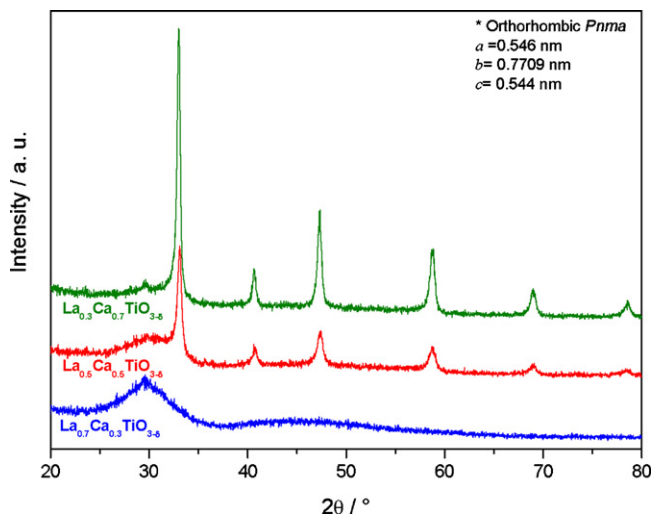


Fig. 5. X-ray diffractograms of $\text{La}_{1-x}\text{Ca}_x\text{TiO}_{3-\delta}$ (for $x = 0.3; 0.5; \text{ and } 0.7$), prepared with a (CA/M) molar ratio of (10/1) and calcined in air at $T = 873 \text{ K}$ for 12 h. Reflections are indexed with the orthorhombic structure. (*) Lattice parameters determined for $\text{La}_{0.3}\text{Ca}_{0.7}\text{TiO}_{3-\delta}$ compound ($a = 0.546 \text{ nm}$; $b = 0.7709 \text{ nm}$; $c = 0.544 \text{ nm}$), based on the orthorhombic crystal structure (space group: $Pnma$).

al. [20] in an aqueous solution of H_2O_2 (30 wt% in water) and ammonia solution (25 wt% in water). After 5 h, a yellow transparent solution of peroxytitanate complexes was obtained. The pH of the solution was adjusted to 4–5 using citric acid ($\text{C}_6\text{H}_8\text{O}_7$, $\geq 99\%$). The required amounts of the other salts ($\text{La}(\text{NO}_3)_3 \cdot 6\text{H}_2\text{O}$ ($\geq 97\%$) and $\text{Ca}(\text{NO}_3)_2 \cdot 4\text{H}_2\text{O}$ ($\geq 98\%$)) were added to this solution. Finally additional citric acid was used as chelating agent to complex the different cations. The citric acid was used in excess with different citric acid/metal cations molar ratio (CA/M = 3/1 or 10/1) in order to prevent precipitation. The citrate precursor was homogenised and polymerised at 353 K for 3 h under continuous stirring. No precipitation was observed which indicates the formation of water soluble polymeric complex compounds.

For the bulk method, the precursor solutions were dried using a rotoevaporator ($T = 343 \text{ K}$; $p = 15 \text{ mbar}$) to promote the forma-

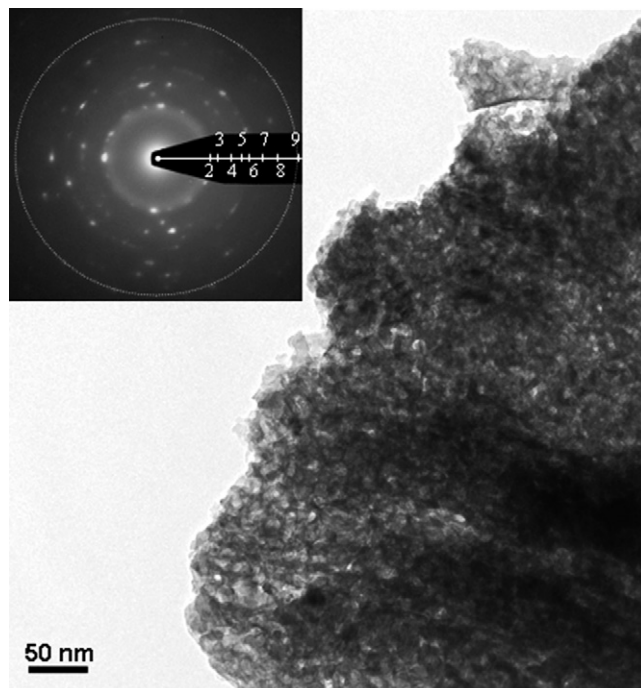


Fig. 7. TEM micrograph picture of $\text{La}_{0.5}\text{Ca}_{0.5}\text{TiO}_{3-\delta}$ calcined at $T = 873 \text{ K}$. The ring pattern is indexed according to the numbers of Table 2.

tion of a viscous gel. The initial thermal decomposition of the precursors was carried out at 573 K for 4 h. The resulting amorphous xerogels were milled and calcined in ambient atmosphere. A few mg of the expanded xerogels were collected at 423 K to determine the thermal decomposition process.

Microdroplets of the same citrate precursor were heat treated in an aerosol process using USC. The precursor solution (0.5 M) was nebulized with a piezoelectric transducer at a frequency of 1.7 MHz in a flow of air (5 L/min). The droplets of citrate precursor were transported into a high temperature reactor ($T_{\text{furnace}} = 1023 \text{ K}$) to obtain perovskite particles. The fine oxide particles were collected in a glass fibre filter heated at 423 K with an average production rate of 200 mg/h.

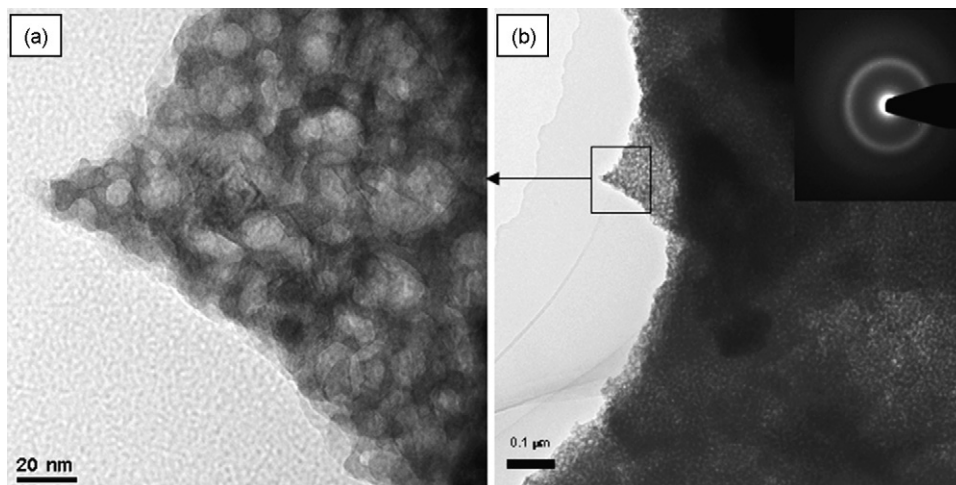


Fig. 6. (a and b) TEM micrograph pictures of $\text{La}_{0.7}\text{Ca}_{0.3}\text{TiO}_{3-\delta}$ calcined at $T = 873 \text{ K}$.

Table 1
Specific surface area and composition of $\text{La}_{1-x}\text{Ca}_x\text{TiO}_{3-\delta}$ synthesised by different synthesis routes

Materials	Synthesis preparation methods	Specific surface area (m^2/g)	Experimental composition (%) ^a	
			La content	Ca content
$\text{La}_{0.7}\text{Ca}_{0.3}\text{TiO}_{3-\delta}$	<i>Chimie douce</i> synthesis route	21	0.72 ± 0.01	0.28 ± 0.01
$\text{La}_{0.5}\text{Ca}_{0.5}\text{TiO}_{3-\delta}$	decomposed by bulk method	31	0.55 ± 0.01	0.45 ± 0.01
$\text{La}_{0.3}\text{Ca}_{0.7}\text{TiO}_{3-\delta}$	(calcined at 873 K)	49	0.25 ± 0.02	0.75 ± 0.02
$\text{La}_{1-x}\text{Ca}_x\text{TiO}_{3-\delta}$ (for $x=0.3; 0.5; 0.7$)	<i>Chimie douce</i> synthesis using the USC process (calcined at T_{furnace} : 1023 K)	50–60	–	–
$\text{La}_{1-x}\text{Ca}_x\text{TiO}_{3-\delta}$ (for $x=0.3; 0.5; 0.7$)	Solid-state reaction method (calcined at 1673 K)	1–2	–	–

^a The experimental composition is evaluated by EDS in situ in conventional TEM.

The thermal decomposition of different precursors was studied using a Netzsch STA 409 CD thermobalance coupled to a mass spectrometer (MS). The Netzsch QMS 403 C Aëlos mass spectrometer allows to identify gaseous reaction products released during the decomposition. Simultaneously recorded thermogravimetric (TG) and differential thermal analysis (DTA) was carried out in reactive atmosphere (80% helium, purity: 5.5 and 20% oxygen, purity: 2.5) or in inert atmosphere with a heating rate of 2 K/min between 300 K and 1273 K. The infrared spectroscopy (IR) was performed using a Fourier transform-infrared spectrometer BIO RAD FTS 175C in the spectral range between $\nu = 3500 \text{ cm}^{-1}$ and 500 cm^{-1} . Phase purity and crystal structure of the products were identified by X-ray diffraction (XRD) with a PANanalytical X'pert diffractometer using $\text{Cu K}\alpha$ radiation. The surface area of the powders was measured with a Quantachrome 3000 by nitrogen adsorption using the Brunauer, Emmet and Teller (BET) method. Prior to adsorption the samples were degassed at 573 K. The morphology of the calcined powders was studied with a scanning electron microscope (SEM) LEO JSM-6300F. The crystal structure of samples was studied by electron diffraction (ED) and high resolution TEM (HREM) imaging using a Philips CM30 transmission electron microscope (TEM). The composition was also analyzed locally by energy dispersive X-ray spectroscopy (EDS) in the range of 30 nm.

3. Results and discussion

Perovskite-type titanate phases were synthesised by the *chimie douce* method. In this cationic complexation technique, the decomposition of the reactive organic–inorganic network results in short diffusion pathways of the different cations [16].

The IR spectrum of the (La,Ca)Ti-citrate precursor at $T=423 \text{ K}$ (Fig. 1) illustrates the organic structure related to the metal complex. The bands at $\nu = 1700 \text{ cm}^{-1}$, 1405 cm^{-1} and 1295 cm^{-1} are ascribed to the carboxylic acid functions of the free citric acid [21]. The broad band around $\nu = 3200 \text{ cm}^{-1}$ can be attributed to the bonded hydroxide stretches [21]. Absorption bands of the carboxylate ions at $\nu = 1560 \text{ cm}^{-1}$ and 1410 cm^{-1} [22] are also observed. The metal-citrate complexes are identified by the characteristic C–O stretch of the α -hydroxy group from the citric acid coordinated to the metal ion at $\nu = 1080 \text{ cm}^{-1}$ [23]. The citric acid functional groups form an organic–inorganic network with the cations as confirmed by the IR data.

The thermal decomposition of the (La,Ca)Ti-citrate xerogel (predried at $T=423 \text{ K}$) was performed for the whole series of compounds in the system $\text{La}_{1-x}\text{Ca}_x\text{TiO}_{3-\delta}$ ($x=0.3; 0.5; 0.7$). All samples show similar decomposition behaviour. Four different thermal steps occur below $T=793 \text{ K}$ as represented by the TG/DTA and DTG profiles (Fig. 2(a and b)). The decomposition

Table 2
Experimental measurements of d_{hkl} from ring diffraction patterns of $\text{La}_{0.5}\text{Ca}_{0.5}\text{TiO}_{3-\delta}$ (Fig. 7), $\text{La}_{0.3}\text{Ca}_{0.7}\text{TiO}_{3-\delta}$ (Fig. 9) and the corresponding hkl

No.	hkl Pseudocubic	hkl Orthorhombic	d_{hkl} (nm) $\text{La}_{0.5}\text{Ca}_{0.5}\text{TiO}_{3-\delta}$	d_{hkl} (nm) $\text{La}_{0.3}\text{Ca}_{0.7}\text{TiO}_{3-\delta}$
0	100	020, 101	–	0.390
1	110	200, 121, 002	0.27	0.273
2	111	220, 022	0.22	0.220
3	200	040, 202	0.19	0.191
4	210	222, 311	0.17	0.17
5	211	321, 240, 042	0.15	0.154
6	220	400, 242, 004	0.14	0.136
7	310	402, 161, 323, 204, 430, 412	0.12	0.119
8	222	440, 044, 432, 234	0.11	0.110
9	321	442, 244, 361, 163	–	0.101
10	400	080, 404	–	0.095

To establish the correspondence, simulation of the diffraction was made by JEMS software [30] (with orthorhombic structure, $Pnma$, $a=0.546 \text{ nm}$, $b=0.7709 \text{ nm}$, $c=0.544 \text{ nm}$).

starts above $T=423$ K with a partial decomposition of the organic material leading to a weight loss of 18.6 wt%. During this first step (at 423 K $< T < 523$ K), a release of H_2O (m/z 18), CO (m/z 28), O_2 (m/z 32), CO_2 (m/z 44) and citric acid fragments $\text{C}_2\text{H}_2\text{O}_2^+$ (m/z 58) is detected by mass spectrometry (Fig. 3(a and b)). The loss of CO_2 can be attributed to the cracking of the carboxylic acid function group of the citric acid. These gas emissions result of the xerogel decomposition. On the IR spectrum at $T=523$ K, the disappearance of the different organic species (carboxylic acid function, bonded hydroxide, carboxylate ions and metal-citrate complex) confirms the decomposition process. In the same temperature region, under inert atmosphere, citric acid fragments, CO_2 and H_2O emissions are observed as well. The CO_2 emission under inert atmosphere allows us to conclude that CO_2 is released due to the decomposition of the citric acid and not as a result of a combustion reaction.

During the second step (at 523 K $< T < 658$ K), the xerogel network is modified as indicated by the IR spectra. The absorption bands of the organic fragments disappear completely at $T=623$ K. The loss of the metal–citrate complex band ($\nu = 1080$ cm^{-1}) results in the destruction of the chelating citrate ligands coordinated to the metal ions. The thermal decomposition causes a weight loss of 23.4 wt% which has a slower reaction rate (from 0.15 wt%/min to 0.50 wt%/min) than the previous step (maximum of 0.75 wt%/min) as indicated by the DTG curve (Fig. 2(b)). Gas emissions of H_2O and CO_2 are recorded by mass spectrometry (Fig. 3(a)). This molecular reorganisation includes a decomposition process leading to the destruction of the direct sphere coordinated to the metal ions.

A strong exothermic event occurs in the third temperature region (at 658 K $< T < 793$ K) leading to the largest weight loss of 52.2 wt%. A release of H_2O , NO_2 , CO and CO_2 (Fig. 3(a and b)) is attributed to the destruction of the organic residue inducing the exothermal reaction. No consumption of O_2 is detected by mass spectrometry during this step. However, a self-oxidation process can be involved to oxidise the precursor. The peroxogroups formed during the dissolution of Ti metal are well suitable to act as the oxidising agent. The presence of carbonate ions CO_3^{2-} is identified from $T=773$ K (Fig. 1) by IR data due to the vibrations at $\nu = 1460$ cm^{-1} , 1060 cm^{-1} and 860 cm^{-1} [22] and highlights the presence of intermediate species. In presence of CO_2 , the cation carbonization appears more favourable than the direct oxidation [24]. The formation of intermediate species occurs probably due to a gas–solid reaction between the released CO_2 and the precursor. In contrast, under inert atmosphere, the DTA signal shows a broad endothermic peak. The precursor undergoes a similar process of self-oxidation due to the presence of peroxogroups. However, under inert atmosphere a reduction reaction seems to be more favourable than the precursor oxidation. The broad endothermic event results from overlapped processes including the precursor reduction under inert atmosphere. Thus, a gradual reduction of the residual material takes place and is not completed at 1273 K.

Between $T=793$ K and 1023 K further small weight losses (0.5 wt%) occur. During this last decomposition stage, no significant CO_2 emission is detected. Nevertheless weak reflections of the perovskite phase can be observed by XRD after heating

at $T=873$ K (Fig. 4). These perovskite reflections are mainly overlapped by broad peaks resulting from the amorphous part. The pure desired perovskite phase is identified by XRD after annealing at $T=973$ K. The perovskite crystallinity improves with thermal treatment and the thermal stability is confirmed by constant weight up to $T=1273$ K. The carbonate groups seem to be stable until $T=823$ K even after applying an isothermal step for 4 h at $T=673$ K. The presence of this intermediate species influences the formation of a pure perovskite phase.

The (La, Ca)Ti-citrate precursor was prepared with different citric acid/metal cations molar ratio (CA/M). The perovskite

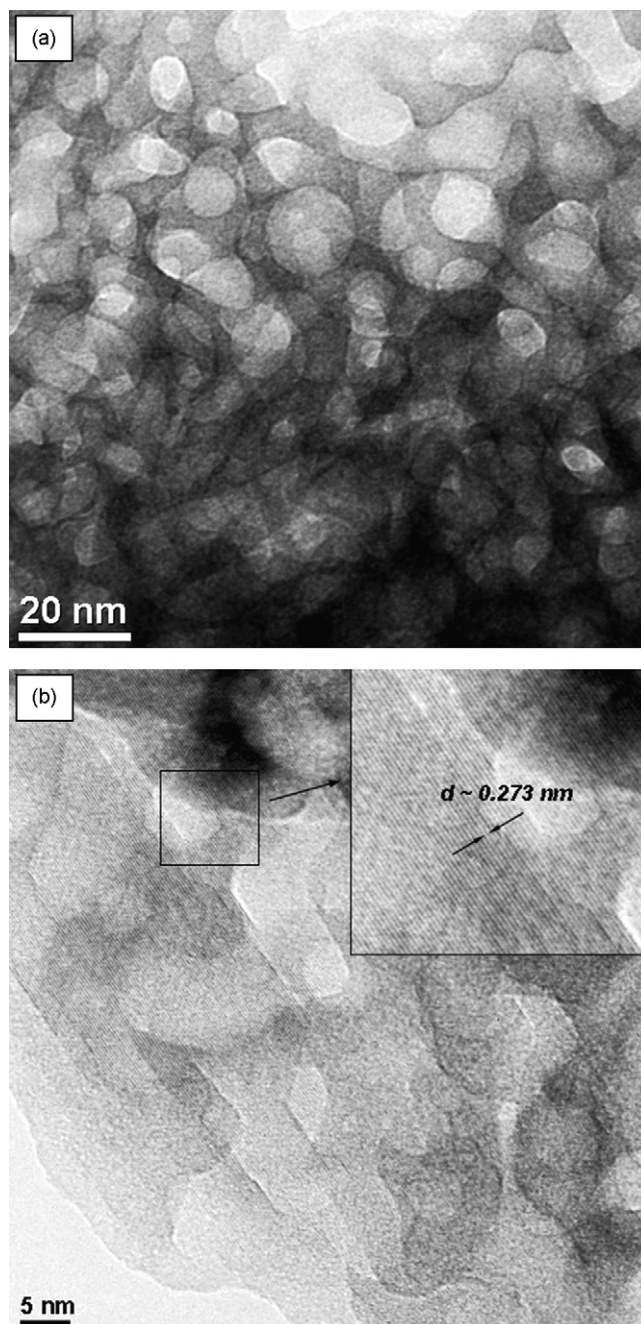


Fig. 8. (a) TEM pictures and (b) HREM images of $\text{La}_{0.5}\text{Ca}_{0.5}\text{TiO}_{3-\delta}$ calcined at $T=873$ K.

phase formation is achieved at $T = 873$ K when the CA/M molar ratio was set to 10/1, as shown on the XRD pattern (Fig. 4). At the same calcination temperature, weak perovskite reflections are observed (as shows by the arrows) for the precursor prepared with a CA/M = 3/1. This compound is partly amorphous. The perovskite-type titanate phase is obtained as well at higher heating temperature (at $T = 973$ K). The citric acid excess supports the complete complexation of cations and an increase of CA/M molar ratio affect directly the exothermic event. More organic material is thermally decomposed which provides higher exothermic reaction energy and therefore leads to a rise of the local temperature during the combustion. The crystallinity is visibly improved during the phase formation due to the crystal growing enhancement.

Different compositions of $\text{La}_{1-x}\text{Ca}_x\text{TiO}_{3-\delta}$ (with $x = 0.3$; 0.5; and 0.7) calcined at $T = 873$ K are described concerning their microstructure, phase formation and their correlations. The XRD patterns (Fig. 5) of the three compounds indicate different crystalline character after heat treatment at 873 K. The cationic composition was evaluated by EDS in a TEM (Table 1).

The La-rich compound ($\text{La}_{0.7}\text{Ca}_{0.3}\text{TiO}_{3-\delta}$) is amorphous as indicated by the broad reflections in the XRD pattern (Fig. 5) and the TEM micrographs (Fig. 6(a and b)). The diffraction pattern inserted in Fig. 6(b) displays one ring created by the diffused scattering. This ring is spread around $d_{110} \sim 0.27$ nm that indicates the sample is in the first stage of the perovskite crystal growth. The porous microstructure of the La-rich compound is characterized by tunnel-like shape channels at $T = 873$ K.

The inserted diffraction pattern (in Fig. 7) of the $\text{La}_{0.5}\text{Ca}_{0.5}\text{TiO}_{3-\delta}$ compound shows a combination of diffraction spots with discontinuous rings from the polycrystalline part and spread rings due to the diffuse scattering. The diffraction pattern (in Fig. 7) is indexed with the orthorhombic structure

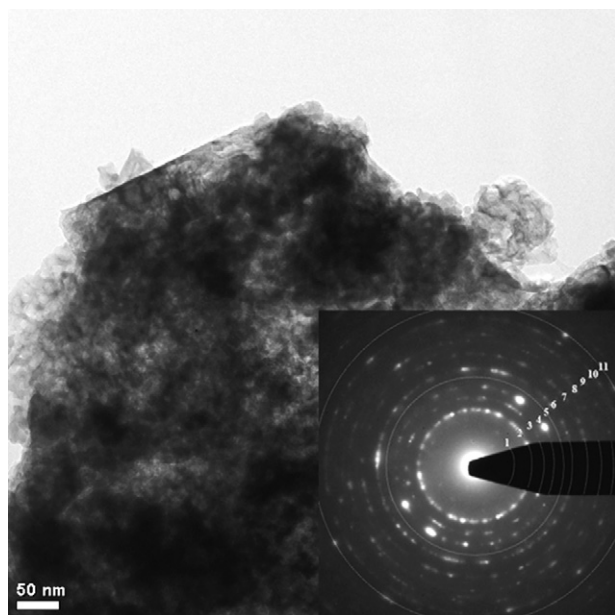


Fig. 9. TEM images of $\text{La}_{0.3}\text{Ca}_{0.7}\text{TiO}_{3-\delta}$ calcined at $T = 873$ K. The inset presents the diffraction pattern of the selected area which is indexed as orthorhombic crystal structure (see Table 2).

(space group: $Pnma$) [25,26] (Table 2). The XRD pattern of the $\text{La}_{0.5}\text{Ca}_{0.5}\text{TiO}_{3-\delta}$ sample also presents reflections of the perovskite structure with broad peaks resulting from the amorphous part. These studies confirm that the $\text{La}_{0.5}\text{Ca}_{0.5}\text{TiO}_{3-\delta}$ compound exhibits amorphous regions mixed with crystalline domains. The microstructure of the amorphous zone is formed by round-shaped channels as shown in Fig. 8(a). In contrast, the microstructure of the crystalline area (Fig. 8(b)) presents open hexagonal channels with straight walls which are well-delimited by $\{110\}$ planes.

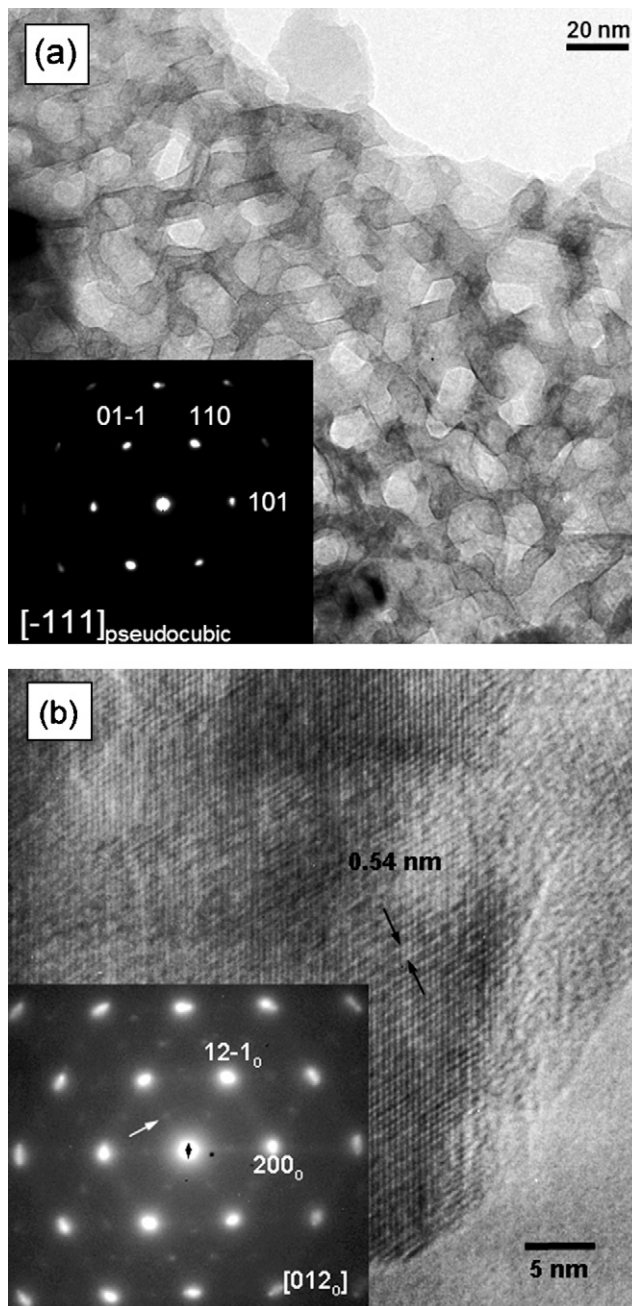


Fig. 10. (a) TEM image of the microstructure and (b) HRTEM image of $\text{La}_{0.3}\text{Ca}_{0.7}\text{TiO}_{3-\delta}$ calcined at $T = 873$ K. The diffraction patterns inserted in (a and b) are indexed either as (a) pseudocubic or as (b) orthorhombic crystal structure.

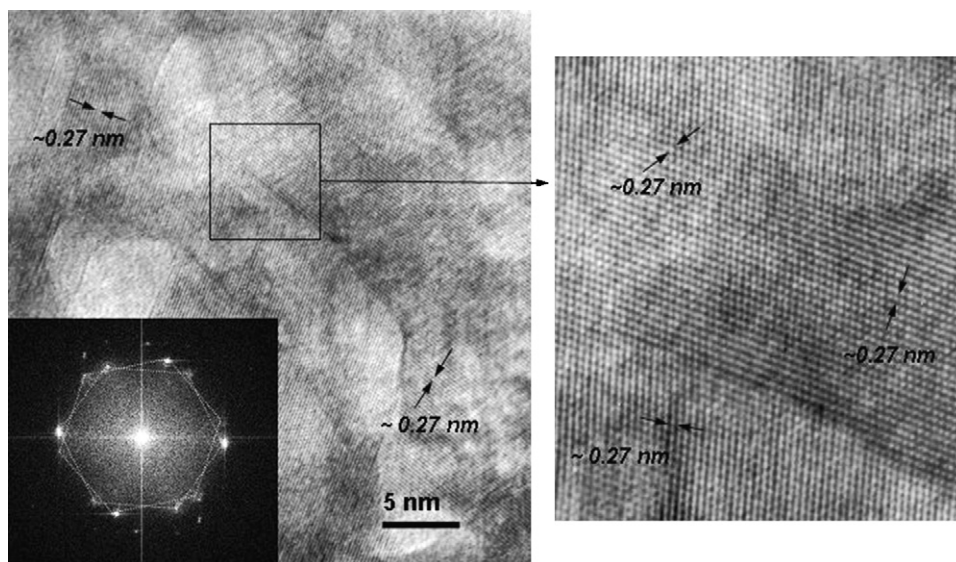


Fig. 11. HREM images of the $\text{La}_{0.3}\text{Ca}_{0.7}\text{TiO}_{3-\delta}$ calcined at $T=873\text{ K}$ (inset: fast Fourier transformation (FFT) of the HREM image which exhibits diffraction patterns of overlapped grains oriented on the $[-1\ 1\ 1]$ zone axis).

The Ca-rich sample ($\text{La}_{0.3}\text{Ca}_{0.7}\text{TiO}_{3-\delta}$) is crystalline as shown by the XRD pattern and the TEM data. On the diffraction pattern (Fig. 9), defined rings are formed by diffraction spots. No diffuse scattering is observed. The ring pattern can be indexed with the orthorhombic structure (space group: $Pnma$) [25,26] (Table 2). The hkl can be indexed as pseudocubic or orthorhombic crystal structure. The detailed microstructure (Fig. 10(a)) presents open channels limited by straight $\{1\ 1\ 0\}$ planes. The HRTEM image (Fig. 10(b)) exhibits the crystalline domains in the Ca-rich compound. The diffraction patterns inserted in Fig. 10(a and b) are indexed as (a) pseudocubic or (b) orthorhombic structure. The extra spots indicated by an arrow on the pattern (figure (b)) confirm the orthorhombic character of the compound. The HREM images (Fig. 11) show in detail the channel delimited by $\{1\ 1\ 0\}$ planes. The fast Fourier transformation (FFT) of the micrograph contains mainly two overlapped diffraction patterns of different grains with zone axis $[-1\ 1\ 1]$ rotating of a few degrees to each other. HREM images with a larger magnification allows to see in detail the zone axis $[-1\ 1\ 1]$ of the structured perovskite walls. The crystalline mesoporous structure will be tested as catalytic materials in future experiments.

The cationic composition in the perovskite-type titanate phases influences the phase formation and the specific surface area as well (Table 1). Higher calcium content allows obtaining crystalline phases at lower calcination temperature. After calcination at $T=873\text{ K}$, the perovskite-titanate particles present different crystal growth stages depending on the cationic composition. The microstructure of the crystalline perovskite-type titanate phases is formed by hexagonal channels of 13–20 nm diameter. The BET isotherms (not shown here) present a hysteresis which is typical for porous materials. The N_2 isotherm is of type IV and accompanied by a type H1 hysteresis loop, according the IUPAC classification [27]. The pore size distribution function is calculated assuming the BJH model and confirms the porous structure found by electron microscopy. A

pore radius of 16 nm is revealed with a deviation of less than 7 nm. The channel-like structures reveal a relatively large surface area and porosity of the oxide. This morphology presents a good exposed surface area which favours the gas exchange in catalytic processes. The presence of the well-defined channels creates a mesoporous morphology which enlarges the exposed surface area compared to the amorphous tunnel-like shape compounds. Higher specific area is achieved with crystalline perovskite-type material due to the specific hexagonal-like shape morphology. The partly or completely amorphous compounds have to be calcined at higher temperatures to favour the crystallisation and therefore promote a defined mesoporous structure as well. Fine agglomerated and partly-sintered particles are obtained by bulk thermal decomposition of the citrate precursor (Fig. 12). Tiny pores between agglomerates particles are formed due to the gas evolution released during the bulk thermal decomposition. The

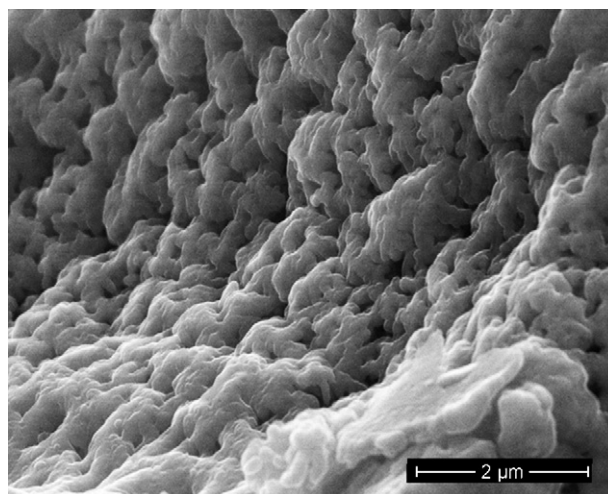


Fig. 12. SEM micrograph picture of $\text{La}_{0.3}\text{Ca}_{0.7}\text{TiO}_{3-\delta}$ perovskite particles synthesised by bulk thermal treatment at $T=1273\text{ K}$.

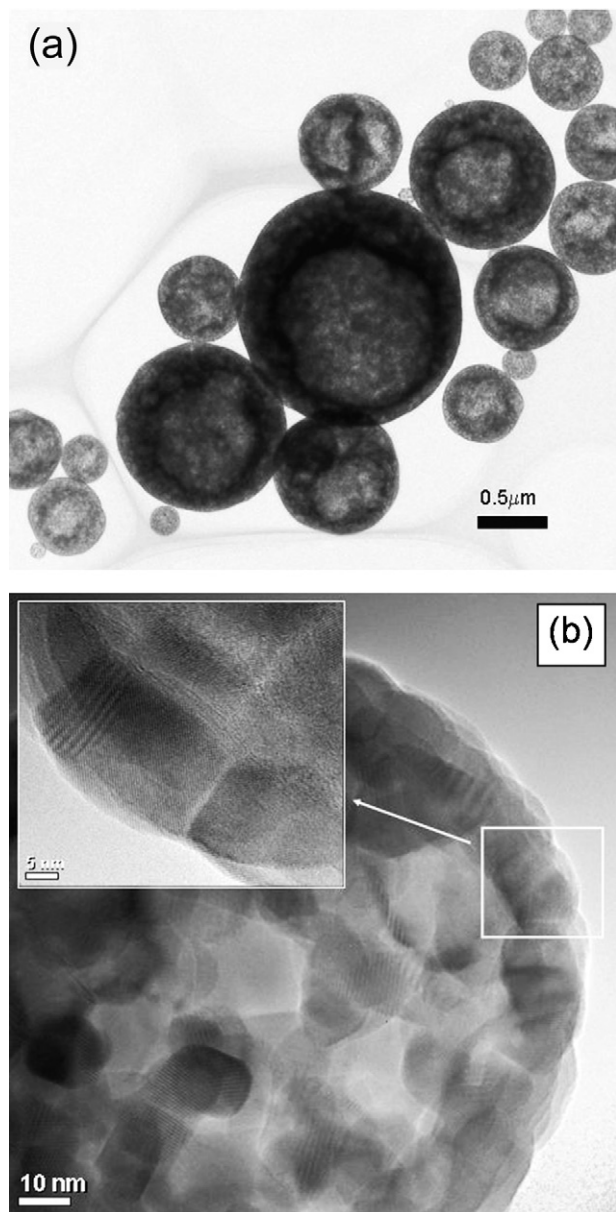


Fig. 13. (a and b) TEM images of $\text{La}_{0.1}\text{Ca}_{0.9}\text{TiO}_{3-\delta}$ perovskite spheres achieved by USC (at $T_{\text{furnace}} = 1173 \text{ K}$). The inset in (b) presents an HRTEM image showing the lattice fringes of the perovskite grains.

partly agglomerated powders show a homogeneous and uniform grain size distribution. A sintering effect supports the growth of the agglomerated particles at higher calcination temperatures.

As an alternative synthesis method the citrate precursor can be decomposed using a continuous USC process [28,29]. This spray combustion concept allows to produce one agglomerate of crystallites per droplet of the misted precursor solution in the carrier gas stream. The droplets are transferred into a quartz tube heated at 1173 K. The decomposition of the organic matter initiates an exothermic combustion to form oxide particles. Individual perovskite spheres are formed by USC process as shown on Fig. 13(a). The low resolution TEM image reveals the contrast change from the border to the centre of each sphere. A bright area is observed in the sphere centre where transmitted electrons

would be more scattered if the spheres were dense. This feature shows the evidence of a hollow structure. Fig. 13(b) represents higher magnification of the sphere where small rectangle-like shape crystallites of 15–30 nm length can be observed. In the inset (Fig. 13(b)) the high resolution TEM image presents lattice fringes of the perovskite crystallites.

The USC process leads to smaller perovskite-type titanate particles compared to the particles achieved by bulk thermal decomposition. Well-defined rectangular crystallites which form hollow spheres are obtained by USC method while the bulk thermal decomposition leads to channel-like crystalline structure. All synthesis routes lead to white perovskite particles. Different particle sizes are obtained depending on the synthesis method. Perovskite-type titanate particles prepared by solid state reaction reveal a specific surface area of $1 \text{ m}^2/\text{g}$ while the *chimie douce* synthesis route, using the USC process, leads to particles with $60 \text{ m}^2/\text{g}$ specific surface area. The *chimie douce* synthesis route allows to achieve at lower synthesis temperature smaller particles compared to the conventional solid state reaction method (Table 1). Previous studies on the thermoelectric activities of perovskite-type cobaltates produced by *chimie douce* synthesis route have shown that the thermal conductivity can be reduced to values lower than 1 W/mK [18].

4. Conclusion

The *chimie douce* synthesis methods lead to smaller perovskite particles by decreasing significantly synthesis time and temperature compared to the conventional ceramic route.

The citrate precursor decomposition reveals a stepwise mechanism. The loss of the excess organic matter is followed at higher temperature by a reorganisation of the organic–inorganic network. This molecular rearrangement includes an organic decomposition process leading to the destruction of the direct sphere coordinated to the metal ions. The destruction of the organic residue at higher temperature induces an exothermic reaction. In CO_2 atmosphere, the cationic environment undergoes a carbonisation leading to an intermediate compound belonging to the carbonate or oxycarbonate family. The intermediate species are decomposed at higher temperature to form the perovskite-type phases. The cationic composition of the mixed oxide ($\text{La}_{1-x}\text{Ca}_x\text{TiO}_{3-\delta}$) influences the crystallisation process. Higher calcium content favours the formation of crystalline channel-like structure. The citrate thermal decomposition can be also directly correlated to the perovskite phase formation and the crystalline fraction.

Highly crystalline perovskite particles, synthesised by bulk thermal decomposition of the citrate precursor, reveal hexagonal channel-like morphology. The well-defined crystalline channels create mesopores (13–20 nm diameter) which lead to a larger surface area. The fine porous perovskite particles are evaluated as potential materials for catalytic applications. The specific porous morphology of the perovskite-type titanate phases can be also applied to enhance the thermoelectric properties by decreasing the lattice thermal conduction. The presence of open spaces between the crystallites can reduce the motions of phonons which control the lattice thermal conductivity.

The production of larger quantities of powder is possible by the continuous USC process while the bulk thermal decomposition is a restricted batch method. The USC process, which avoids the particle agglomeration, enhances the specific surface area by a factor 3 compared to the bulk thermal decomposition. Sintered ultrafine perovskite particles achieved by the USC process form hollow sphere shape. The bulk thermal decomposition leads to a mesoporous morphology where the crystalline perovskite grains create defined channels. Different particle size as well as morphology can be fine-tuned by suitable decomposition processes. Knowledge on precursor thermal decomposition allows good control in tailoring the desired morphology of the perovskite phases.

Acknowledgments

The authors would like to thank the Swiss Federal Office of Energy (BFE) and Empa for the financial support. Claudia Schreiner, Benjamin Savreux and Cornelia Seiler are acknowledged for their technical help.

References

- [1] F.S. Galasso, in: F.S. Galasso (Ed.), *Structure, Properties and Preparation of Perovskite-type Compounds*, Pergamon Press Ltd., Oxford, 1969, pp. 60–76.
- [2] S. Canulescu, T. Lippert, H. Grimmer, A. Wokaun, R. Robert, D. Logvinovich, A. Weidenkaff, M. Doebeli, *Appl. Surf. Sci.* 252 (2006) 4599–4603.
- [3] R. Robert, S. Romer, A. Reller, A. Weidenkaff, *Adv. Eng. Mater.* 7 (2005) 303–308.
- [4] I. Terasaki, Y. Sasago, K. Uchinokura, *Phys. Rev. B: Condens. Matter Mater. Phys.* 56 (1997) R12685–R12687.
- [5] A. Reller, A. Weidenkaff, G. Fortunato, O. Becker, G. Bednorz, *Nova Acta Leopoldina* 317 (2000) 47–65.
- [6] K. Koumoto, I. Terasaki, T. Kajitani, M. Ohtaki, R. Funahashi, in: D.M. Rowe (Ed.), *Thermoelectrics Handbook—Macro to Nano*, CRC Press/Taylor & Francis Group, Boca Raton, 2006, pp. 1–13 (Chapter 35).
- [7] D.M. Rowe, in: D.M. Rowe (Ed.), *Thermoelectrics Handbook—Macro to Nano*, CRC Press/Taylor & Francis Group, Boca Raton, 2006, pp. 3–6 (Chapter 1).
- [8] A. Maignan, C. Martin, D. Pelloquin, N. Nguyen, B. Raveau, J. *Solid State Chem.* 142 (1999) 247–260.
- [9] T. Okuda, S. Nakanishi, S. Miyasaka, Y. Tokura, *Phys. Rev. B: Condens. Matter Mater. Phys.* 63 (2001) 1–4.
- [10] R. Robert, L. Bocher, M. Trottmann, A. Reller, A. Weidenkaff, *J. Solid State Chem.* 179 (2006) 3893–3899.
- [11] G.S. Nolas, J. Yang, H.J. Goldsmid, in: T.M. Tritt (Ed.), *Thermal Conductivity—Theory, Properties and Applications*, Kluwer Academic/Plenum Publishers, New York, 2004, pp. 123–152 (Chapter 1.5).
- [12] Ch. Kittel, in: Ch. Kittel (Ed.), *Introduction to Solid State Physics*, eighth ed., John Wiley & Sons, Inc., USA, 2004, pp. 156–159 (Chapter 6).
- [13] I. Matsubara, R. Funahashi, T. Takeuchi, S. Sodeoka, T. Shimizu, K. Ueno, *Appl. Phys. Lett.* 78 (2001) 3627–3629.
- [14] J.M. Thomas, W.J. Thomas, in: J.M. Thomas (Ed.), *Principles and Practice of Heterogenous Catalysis*, VCH, Weinheim, 1997, pp. 340–344 (Chapter 5.2).
- [15] H. Tanaka, M. Misono, *Curr. Opin. Solid State Mater. Sci.* 5 (2001) 381–387.
- [16] A. Weidenkaff, *Adv. Eng. Mater.* 6 (2004) 709–714.
- [17] E. Krupicka, A. Reller, A. Weidenkaff, *Cryst. Eng.* 5 (2002) 195–202.
- [18] R. Robert, L. Bocher, B. Sipo, M. Döbeli, A. Weidenkaff, *Prog. Solid State Chem.* (2007), doi:10.1016/j.progsolidstchem.2007.01.020.
- [19] M.P. Pechini, US patent No 3 330 697 (1967).
- [20] E.R. Camargo, E. Longo, E.R. Leite, *J. Sol-Gel Sci. Technol.* 17 (2000) 111–121.
- [21] D. Lin-Vien, N.B. Colthup, W.G. Fateley, J.G. Grasselli, in: D. Lin-Vien, et al. (Eds.), *The Handbook of Infrared and Raman Characteristic Frequencies of Organic Molecules*, Academic Press Inc., San Diego, 1991, pp. 137–141 (Chapter 9).
- [22] D. Hennings, W. Mayr, *J. Solid State Chem.* 26 (1978) 329–338.
- [23] D. Nelis, G. Mondelares, A. Vanhoyland, A. Hardy, K. Van Werde, H. Van den Rul, M.K. Van Bael, J. Mullens, L.C. Van Poucke, J. D’Haen, *Thermochim. Acta.* 426 (2005) 39–48.
- [24] H. Fjellvag, O.H. Hansteen, B.G. Tilset, A. Olafsen, N. Sakai, H. Seim, *Thermochim. Acta* 256 (1995) 75–89.
- [25] V. Vashook, L. Vasylechko, M. Knapp, H. Ullmann, U. Guth, *J. Alloys Compd.* 354 (2003) 13–23.
- [26] O.P. Shrivastava, N. Kumar, I.B. Sharma, *Bull. Mater. Sci.* 27 (2004) 121–126.
- [27] K.S.W. Sing, D.H. Everett, R.A.W. Haul, L. Moscou, R.A. Pierotti, J. Rouquerol, T. Siemieniewska, *Pure Appl. Chem.* 57 (1985) 603.
- [28] W. Guo, A.K. Datye, T.L. Ward, *J. Mater. Chem.* 15 (2005) 470–477.
- [29] J.P. Coutures, P. Odier, C. Proust, *J. Mater. Sci.* 27 (1992) 1849–1856.
- [30] P.A. Stadelmann, *Ultramicroscopy* 21 (1987) 131–145.